Insights into Cytochrome P450 Enzymes Catalyzed Defluorination of Aromatic Fluorides

DOI:
10.1002/anie.202310785

Document Version
Accepted author manuscript

RESEARCH ARTICLE

Insights into Cytochrome P450 Enzymes Catalyzed Defluorination of Aromatic Fluorides

Yi Zhang,[a,b] Thirakorn Mokkawes,[a,b] and Sam P. de Visser[a,b]*

[a] Mr Y. Zhang, Dr T. Mokkawes, Dr S.P. de Visser
Manchester Institute of Biotechnology
The University of Manchester
131 Princess Street, Manchester M1 7DN, United Kingdom
E-mail: sam.devisser@manchester.ac.uk
[b] Mr Y. Zhang, Dr T. Mokkawes, Dr S.P. de Visser
Department of Chemical Engineering
The University of Manchester
Oxford Road, Manchester M13 9PL, United Kingdom

Supporting information for this article is given via a link at the end of the document.

Abstract: The biodegradability of many fluorinated compounds is limited due to the robustness of the C–F bond. Recently, experimental studies suggested the potential involvement of cytochrome P450 enzymes in facilitating aromatic defluorination, raising questions where this can be applied in biocatalysis. Our study offers an in-depth computational examination into the oxidative defluorination process of a drug molecule, mediated by cytochrome P450 Compound I. We explored a large number of potential mechanisms, and identify two competitive low-energy pathways that are initiated with an electrophilic attack on the aromatic ring, and followed by either a 1,2-fluorine shift or a ring-closure to form an epoxide intermediate. Both of these intermediates are shown to react rapidly through defluorination assisted by a solvent proton. Interestingly, defluorination in the vicinity of a heme group may generate a stable iron(III)-fluoride complex, potentially leading to enzyme inactivation.

Introduction

Fluorinated compounds are widely used in the chemical industry as a C–F bond gives it unique properties including often extended lifetime, thermal stability and it makes the compound chemically resistant. These properties make them highly suitable as an insulator. Moreover, in agriculture, fluorinated compounds are extensively used as herbicides and pesticides, while in medicine drug molecules and biotherapies often contain compounds with C–F bonds.[1] In medicine, fluorinated compounds are used as therapies as their enhanced polarity enables better membrane permeability.[1a] Due to their high stability and poor biodegradability, however, these fluorinated compounds are causing environmental pollution.

Generally, in inorganic chemistry, heavy metals are used as catalysts for the activation of C–F chemical bonds.[2] However, in nature, under ambient conditions, the aromatic C–F bond cleavage is challenging as a result of its strong bond energy of the order of 126 kcal mol^{-1}.[3] As such, research is underway to find suitable oxidants for the cleavage of C–F bonds and indeed in recent years, several biomimetic examples have been reported of iron and copper complexes able to activate C–F bonds of substrates.[4] In addition, several enzymes in nature have been identified that are able to cleave aromatic C–F bonds efficiently.[5] In particular, the aromatic amino acid hydroxylases, such as tyrosine hydroxylase, phenylalanine hydroxylase, and tryptophan hydroxylase all readily take fluorinated substrates and react through defluorination.[6] Conversely, fluorinated substrates often lead to a different site of activation as compared to the natural substrate due to differences in substrate binding and electron-donating or electron-withdrawing effects.

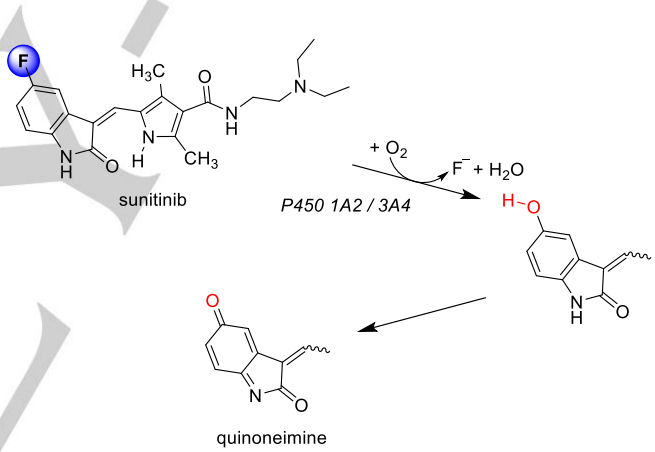

Scheme 1. Activation of sunitinib by P450 1A2 enzymes and products obtained.

In addition to nonheme iron enzymes reacting through oxidative dehalogenation with their substrate, there is scientific evidence that also heme enzymes can be involved in these processes. Firstly, the heme haloperoxidases utilize H_2O_2 on a histidine-ligated heme center and react with aromatic substrates through C–X (X = F, Cl, Br) cleavage to form phenols.[7] Secondly, either wild-type or engineered cytochrome P450 enzymes have been found to react with halogenated arenes through dehalogenation reactions.[8] In particular, a recent study showed that the human liver P450 isozymes P450 1A2 and P450 3A4 were found to react with the sunitinib drug molecule via an oxidative defluorination reaction (Scheme 1).[9] However, this defluorination step activates the drug molecule and converts it into a quinoneimine, which is a toxic metabolite. Details of the mechanism are unknown, and several potential pathways were proposed including an epoxidation reaction of the aromatic ring of sunitinib by P450 1A2 or 3A4 followed by rearrangement to give the phenol and quinoneimine in equilibrium. To understand the process of oxidative defluorination by P450 enzymes we decided to do a computational study into sunitinib activation and its conversion

into a quinoneimine as a model reaction for aromatic defluorination by P450 isozymes. Our studies highlight the catalytic potential of P450 isozymes for oxidative defluorination reactions.

The cytochromes P450 are a large class of heme monooxygenases that typically catalyze oxygen atom transfer reactions to a substrate.[10] They are common in the human body such as the liver where they partake in detoxification reactions of xenobiotics and hence are popular enzymes for studies on drug toxicity.[11] In particular, the P450 1A2 isozymes play an important role in the metabolism of a range of drug molecules in the liver.[12] In general, the P450s utilize dioxygen on an iron(III)-heme and with the help of two external electrons and protons generate an iron(IV)-oxo heme cation radical (Compound I, CpdI) as active species. CpdI reacts with substrates through aromatic or aliphatic hydroxylation of C–H bonds or performs heteroatom activation to convert sulfides into sulfoxides. Although most of the mechanistic details of these reactions have been studied with models previously,[13] little is known about aromatic defluorination by the P450s and whether it would have large-scale potential in biotechnology. An early computational study reported hexachlorobenzene dechlorination mechanisms for a minimal cluster model of P450 CpdI using a porphyrin without side chains and the protein environment ignored.[14] The studies proposed an electrophilic mechanism where the oxygen atom of CpdI attacks one of the carbon atoms of the aromatic ring, which triggers a chlorine 1,2-migration to form a quinone product. The work gave some valuable insights into possible reaction mechanisms, however, since the second-coordination sphere of the substrate and heme were ignored in the models, the work may not be representative of a complex reaction like sunitinib activation by P450 1A2. Moreover, a defluorination process requires the cleavage of a much stronger bond than a dechlorination reaction and consequently a different mechanism may apply. Furthermore, sunitinib is a large and bulky substrate that may not have enough flexibility and mobility to bind under ideal conditions and enables these halide migration steps. Therefore, we decided to explore a large cluster model that takes the substrate binding pocket and hydrogen bonding network into consideration. Our studies reveal a novel pathway via the initial electrophilic addition followed by either a 1,2-fluorine shift or the formation of an epoxide intermediate. Both reaction products then with the assistance of a H_3O^+ ion from the solvent can defluorinate the substrate efficiently.

Results and Discussion

We started the work with a series of molecular dynamics simulations on sunitinib-bound P450 1A2, see Supporting Information for details. To this end, we took the 2HI4 protein databank file (pdb),[15] which is a 1.95 Å resolution monomer structure of the human cytochrome P450 1A2 isozyme with α-naphthoflavone bound. We removed α-naphthoflavone and crystal waters from the pdb structure and added hydrogen atoms under pH 7 conditions. Next, sunitinib was inserted into the protein structure through docking in Autodock Vina;[16,17] however, due to its long size and charged tail, only a few stable sunitinib-bound orientations were found and all have the charged group of the substrate in the same location, namely in hydrogen bonding interaction with the hydroxyl groups of Thr_{118}, Ser_{122} and Thr_{124}. We chose the lowest energy conformation from the docking and set up an enzymatic structure for subsequent MD simulation, see Methods for details. The MD simulation was run for 50 ns and shows that the substrate is tightly bound in the substrate-binding pocket and moves little in position during the MD simulation (Supporting Information). As a matter of fact, most chains stay in the same position during the full MD simulation. Moreover, the root-mean-square deviation (RMSD) of the geometry during the MD simulation converges rapidly (Figure S2, Supporting Information). In all structures, sunitinib remains in the substrate-binding pocket with the C–F bond pointing toward the heme.

Based on the last snapshot of the MD simulation we created large active site cluster models that take the local environment of the substrate and oxidant into consideration and decided to do a quantum chemical study on the chemical reaction mechanism of defluorination of sunitinib by P450 1A2. These large cluster models take the second coordination sphere of the oxidant and substrate into account and have been shown to accurately reproduce experimental rate constants, product distributions and reaction selectivities.[18] Figure 1(a) shows cluster model **I** that was created for sunitinib activation studies. We truncated all side chains of the heme to hydrogen atoms and describe the axial cysteinate as thiolate. The full substrate was included and the α-helix from Asn_{312} until Thr_{321} as well as some shorter peptide chains surrounding the substrate. Overall Model **I** had 367 atoms. We also tested a further expanded model (Model **II**) of 484 atoms that included the protein chains of Ile_{459} and Gly_{460}, the peptide dimer Phe_{226}-Val_{227}, and side chains of Leu_{382} and Pro_{383}. However, the optimized geometries were very close to those found for Model **I**; hence most of the work was done with Model **I**.

It is generally believed that the iron(IV)-oxo heme cation radical intermediate in the catalytic cycle of P450 enzymes, i.e., Compound I (CpdI), is the active oxidant that reacts with the substrate.[10,19] Indeed for $P450_{CAM}$ CpdI was trapped and characterized and shown to react with substrate through hydrogen atom abstraction.[19a] Therefore, a CpdI model (structure **A**) was created with substrate bound, and a geometry optimization was done using Model **I** in the doublet and quartet spin state and Model **II** in the quartet spin state. We initially optimized structure $\mathbf{A}_{\mathrm{I}}$ without constraints, however, that led to large distortions of the protein environment with respect to the MD snapshots. We subsequently fixed seven α-carbon atoms of protein chains as highlighted with a star in Figure 1(a) as well as two nitrogen atoms of the heme to prevent heme rotation. Optimized geometries of the $\mathbf{A}_{\mathrm{I}}$ and $\mathbf{A}_{\mathrm{II}}$ structures are shown in Figure 1(b) and (c). The optimized geometries compare well to cluster models and QM/MM optimized geometries of alternative P450 CpdI isozymes reported previously,[20] and a short Fe–O distance of 1.653 (1.650) Å is obtained in the quartet (doublet) spin state for Model **I** and 1.651 Å for $^4\mathbf{A}_{\mathrm{II}}$. The Fe–S bond is long as expected from the interaction of two second-row elements and the calculated distances match previous results well.[20] An overlay of the two optimized geometries of the doublet and quartet spin reactants gives an almost perfect match with identical geometries and substrate-binding positions. The optimized geometry of the larger cluster model **II** gives distances similar to those for Model **I**; hence we continued the work with the 367-atom model only.

Both doublet and quartet spin states of $^{2,4}\mathbf{A}$ have an electronic configuration with orbital occupation $\delta_{x2\text{-}y2}^2\ \pi^*_{xz}{}^1\ \pi^*_{yz}{}^1\ a_{1u}{}^2\ a_{2u}{}^1$, whereby the a_{2u} electron is up-spin in the quartet spin state and down-spin in the doublet spin state.

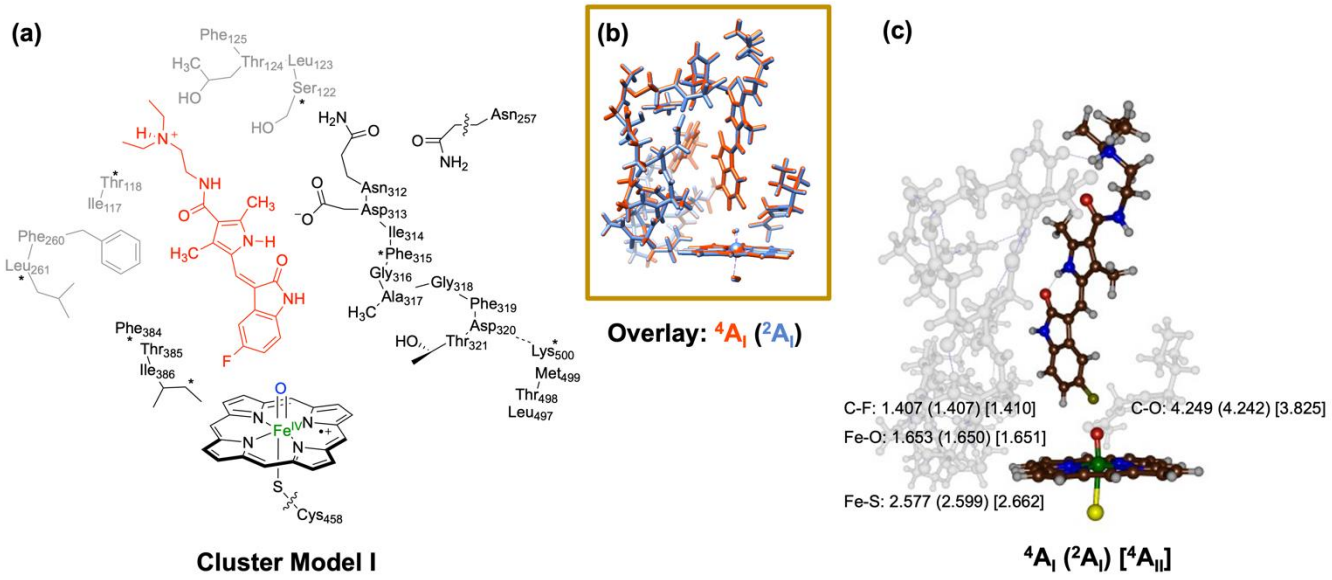

Figure 1. (a) Cluster Model **I** studied in this work. (b) Overlay of the Model **I** optimized geometries ^{4}**A**$_I$ and ^{2}**A**$_I$. Atoms labelled with a star were fixed during the geometry optimizations. (c) Optimized geometries of ^{4,2}**A**$_I$ and ^{4}**A**$_{II}$ with bond lengths in Ångströms.

These molecular orbitals represent the interactions of the metal with its first-coordination sphere ligands. Thus, the occupied orbitals include the nonbonding δ_{x2-y2} orbital, which is a dominant metal 3d orbital in the plane of the heme, and the two antibonding orbitals for the interaction of $3d_{xz}/3d_{yz}$ on iron with $2p_x/2p_y$ on oxygen (π^*_{xz}/π^*_{yz}). Two π^* orbitals on the heme manifold are labeled as a_{1u} and a_{2u}, whereby the latter interacts strongly with a lone pair orbital on the axial sulfur ligand and is highest in energy.[13a,20] The two spin states are close in energy (within 0.2 kcal mol^{-1}) as commonly found for CpdI model complexes and they have the same electronic configuration and orbital occupation. Therefore, multistate reactivity patterns are expected on competing doublet and quartet spin state surfaces.[21] Alternative electronic states were tested in the doublet and quartet spin state but found to be well higher in energy, see Supporting Information.

Next, the oxidative defluorination of sunitinib was studied for the **A**$_I$ model in the doublet and quartet spin states, whereby we explored various potential mechanisms for either phenol or quinoneimine formation, see Scheme 2. The work starts from doublet and quartet CpdI (^{4,2}**A**$_I$) with an electrophilic addition step via transition state **TS1** to form a C–O bond between the aromatic ring of sunitinib and the oxo group in structure **B**. In the optimized geometries of ^{2,4}**A**$_I$ the nearest carbon atom of sunitinib to the oxo group of CpdI is the one containing the C–F bond at a distance of 4.24 Å. Therefore, an electrophilic attack on that carbon atom was explored. By contrast, the adjacent carbon atoms are at a distance more of close to 5 Å from the heme and their activation will require large structural changes, hence these pathways were not investigated here. Although structure **B** is shown as a radical on the substrate in Scheme 2, we also considered the alternative electromer with iron(III) coupled to a substrate cation. Subsequently, from structure **B** bifurcation pathways were tested, namely for the substrate C–F bond cleavage and fluorine transfer to iron to give intermediate **C** via transition state **TS2**, or 1,2-fluorine-migration within the substrate via **TS7** to give the quinone product **H**. In addition, ring-closure via transition state **TS5** to form the epoxide intermediates **F** was explored. As the catalytic cycle of P450 enzymes contains two proton relay steps, we assume a proton shuttle channel into the active site is available for the proton-assisted defluorination steps.[10] Therefore, both structures **F** and **H** with the assistance of a proton from the solvent, i.e., H_3O^+, were studied for defluorination of the substrate to form the quinoneimine products (**G**) and HF. In addition, product formation pathways from the structures **C** were explored. Firstly, we added an H_3O^+ and water molecule to model **C**, i.e., **C**•(H_2O)(H_3O^+), to study the next step for proton transfer to the oxygen atom to give the phenol product **D** via transition state **TS3**. Secondly, a reaction channel leading to quinoneimine products **D'** were tested for proton abstraction from the imine group from structure **C**. Thus, three water molecules were added to structure **C** nearby the imine group, i.e., model **C**•(H_2O)$_3$, whereby we investigated the proton transfer from the substrate N–H group to water and the subsequent desaturation to give quinoneimine via **TS3'**. Finally, we tested fluoride release from the iron center in **C** to form products **E**. Full details of the calculated mechanisms and pathways and the optimized structures and constraint geometry scans are shown in the Supporting Information, while we focus on the main trends here.

Let us start the mechanistic investigations that focus on the results of the conversion of ^{4,2}**A**$_I$ into ^{4,2}**C**$_I$ and the various electromers involved in the process. Density functional theory (DFT) calculated potential energy profile for the conversion of **A** into **C** is given in Figure 2. Several C–O bond activation transition

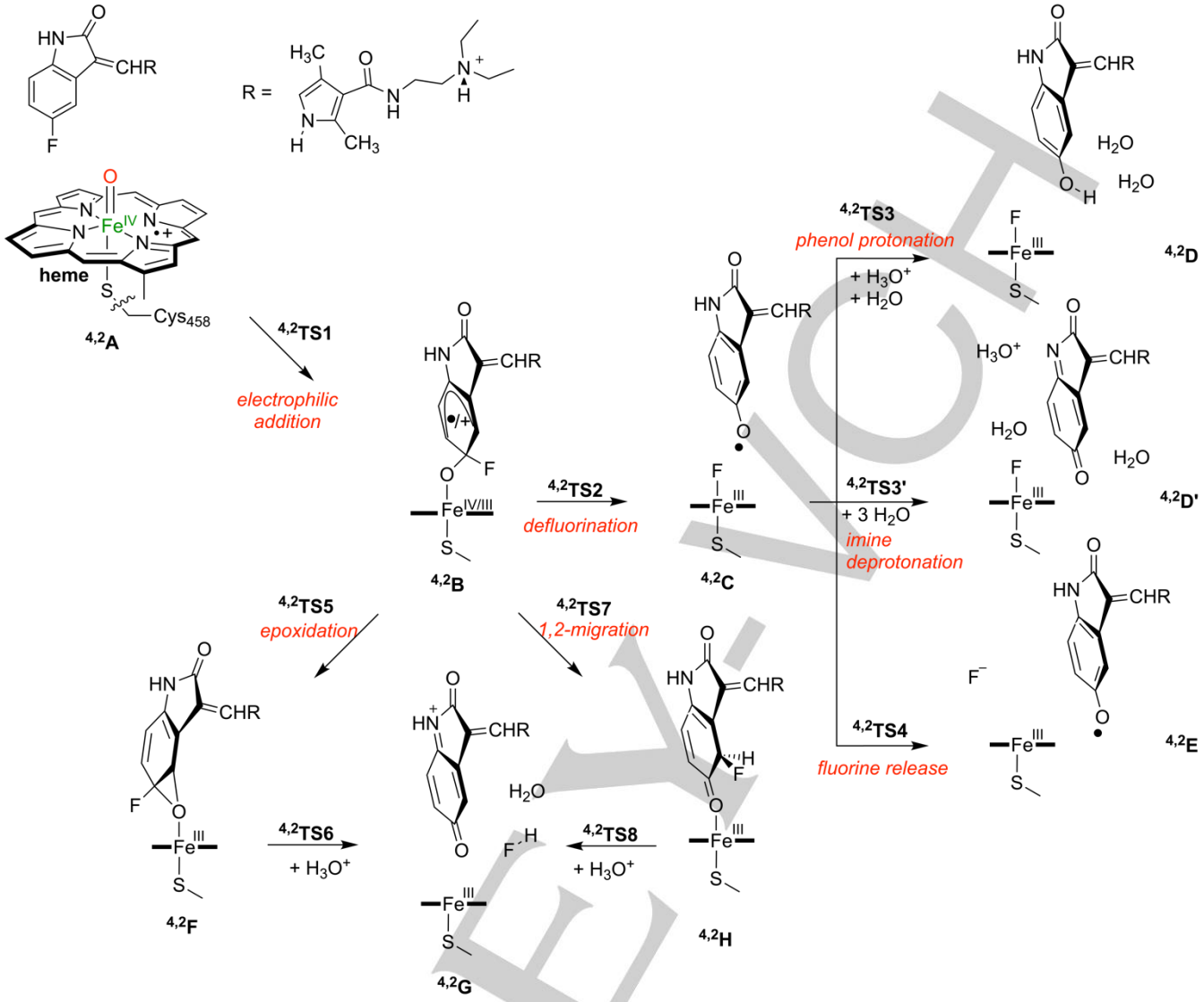

Scheme 2. Reaction mechanisms studied in this work. Protein residues in the model have been hidden.

states were characterized; however, the two lowest in energy had an iron(IV) group and closed-shell heme coupled to a substrate radical with barriers of $\Delta G^{\ddagger}$ = 12.3 kcal mol^{-1} in the doublet spin state and $\Delta G^{\ddagger}$ = 15.0 kcal mol^{-1} on the quartet spin state. Both states have electronic configurations of $\delta_{x2\text{-}y2}^2\ \pi^*_{xz}{}^1\ \pi^*_{yz}{}^1\ a_{1u}^2\ a_{2u}^2\ \pi_{Sub}{}^1$, whereby the π_{Sub} orbital represents a π-orbital on the substrate manifold. The π_{Sub} orbital is occupied with an up-spin electron in the quartet spin state and a down-spin electron in the doublet spin state, while the π^*_{xz} and π^*_{yz} orbitals in both cases are occupied with one up-spin electron. These two states relax to the iron(IV)-type radical intermediates $^{4,2}\mathbf{B}_{IV}$ that are at ΔG = –1.0 and 2.7 kcal mol^{-1} with respect to the reactant complexes in the quartet and doublet spin states, respectively.

An analysis of the group spin densities and orbital occupations was done to assign electromeric states for all transition states and local minima along the mechanism. Thus, the group spin densities in ^{4}**TS1**$_{IV}$ show a decrease in the heme and axial ligand to 0.45, whereas $^4\mathbf{A}_I$ had a spin of 0.98 on the sum of those groups. At the same time, the spin density on the Fe–O moiety remains above 2 for ^{4}**TS1**$_{IV}$ and $^4\mathbf{B}_{IV}$. Similar patterns are seen for ^{2}**TS1**$_{IV}$ and $^2\mathbf{B}_{IV}$ that give a negative spin on the substrate while retaining a spin of about 2 on the Fe–O group. We also located alternative radical intermediates with an iron(III) oxidation state and a radical on the heme through an unpaired electron in the a_{2u} orbital, namely electronic states ^{4,2}**TS1**$_{III}$. In ^{4}**TS1**$_{III}$ spin is lost on the Fe–O group and the spin on the heme and axial ligand stays above a value of 1. As such, the ^{4}**TS1**$_{III}$ structure corresponds to an electronic configuration of $\delta_{x2\text{-}y2}^2\ \pi^*_{xz}{}^2\ \pi^*_{yz}{}^1\ a_{1u}^2\ a_{2u}{}^1\ \pi_{Sub}{}^1$. These iron(III)-type **TS1** structures are high in energy and were found to be above >29 kcal mol^{-1} in energy with respect to the reactant complex. Therefore, at room temperature, we do not expect these to take a role of importance in the reaction mechanism. Using minimal cluster models, the iron(IV)-type radical intermediates are usually lowest in energy,[22] but examples have been identified where the second-coordination sphere effects and substrate positioning restrictions and bring the iron(III) and iron(IV) states close in energy.[22,23] Interestingly, $^{2,4}\mathbf{B}_{IV}$ structures are not the lowest energy **B**-type intermediates along the reaction mechanism as the electromers $^{2,4}\mathbf{B}_{cat}$ were located as well and had a ΔG = –10.4 (doublet) and –12.9 (quartet) kcal mol^{-1} with respect to reactants.

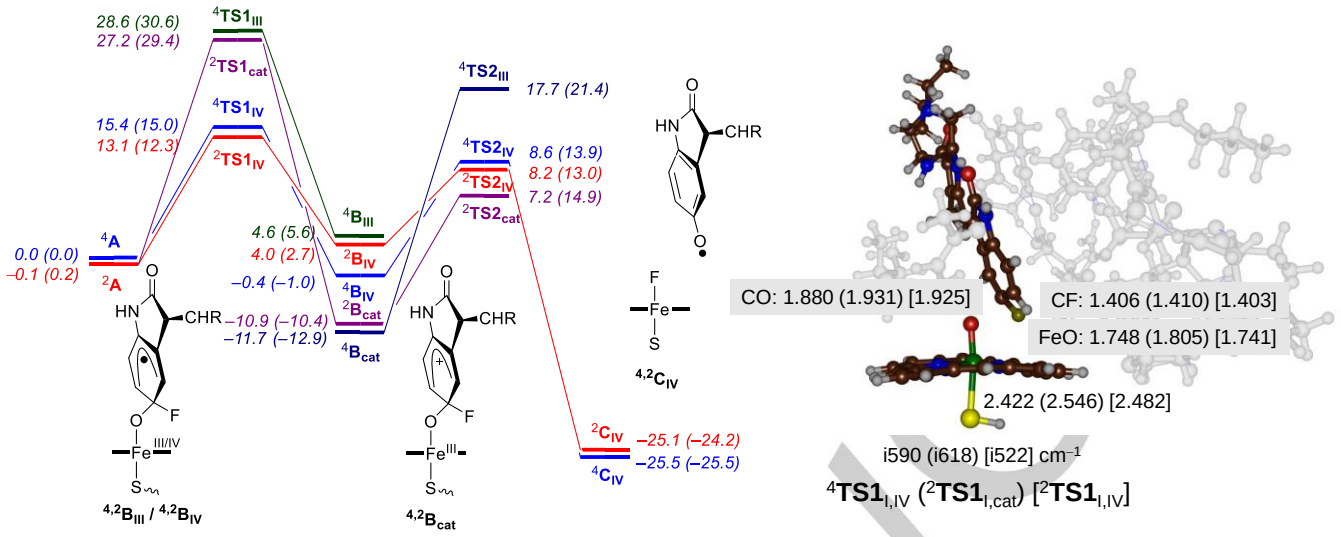

Figure 2. Sunitinib defluorination reaction via electrophilic pathways by a large CYP 1A2 cluster model of 367 atoms as calculated with DFT approaches. Energies are UB3LYP/BS2//UB3LYP/BS1 values in kcal mol^{-1} corrected with zero-point energies, while free energies at 298 K are in parenthesis. Optimized transition state structures give bond lengths in Å and the imaginary frequency in cm^{-1}.

The ^{2}**B**$_{cat}$ intermediate has electronic configuration $\delta_{x2\text{-}y2}^{2}$ $\pi^{*}_{xz}{}^{2}$ $\pi^{*}_{yz}{}^{1}$ $a_{1u}{}^{2}$ $a_{2u}{}^{2}$ $\pi_{Sub}{}^{0}$, and an iron(III) with a closed-shell heme and a cation located on the substrate. Hence, the formation of ^{2}**B**$_{cat}$ from ^{2}**A**$_{I}$ corresponds to a double electron transfer from the substrate to CpdI during the C–O bond formation. This structure has a spin of 1.15 on iron, negligible spin density on the oxygen and fluorine atoms, and little spin on the substrate (<0.10). The ^{4}**B**$_{cat}$ intermediate has electronic configuration $\delta_{x2\text{-}y2}^{2}$ $\pi^{*}_{xz}{}^{1}$ $\pi^{*}_{yz}{}^{1}$ $\sigma^{*}_{z2}{}^{1}$ $a_{1u}{}^{2}$ $a_{2u}{}^{2}$ $\pi_{Sub}{}^{0}$, representing an iron(III) with a closed-shell heme and a cation located on the substrate. It has a spin density of 2.54 on the Fe–O group, while some spin is also located on the heme and thiolate ligands (ρ = 0.46) due to the single occupation of the σ^{*}_{z2} orbital, which is a mixed 3d$_{z2}$(Fe) with 3p$_{z}$(S) antibonding orbital. Clearly environmental perturbations from the second coordination sphere stabilize the ^{2,4}**B**$_{cat}$ structure and make them the most stable **B**-type intermediates even though the radical-type transition states ^{4,2}**TS1**$_{IV}$ are lowest for the electrophilic addition. In particular, the transition states leading to the cationic intermediates are >ΔG = 29 kcal mol^{-1} above reactants and hence these barriers are well higher in energy than the radical-type transition states ^{2,4}**TS1**$_{IV}$. However, it is possible that during the lifetime of ^{2,4}**B**$_{IV}$ states an internal electron transfer takes place, thereby converting the structures into ^{2,4}**B**$_{cat}$. Thus, ^{2}**TS1**$_{cat}$ has a spin of 1.19 on iron, a spin of –0.61 for the sum of the heme and axial thiolate ligand, and a spin of 0.40 on the substrate. Consequently, substantially more electron transfer has taken place in ^{2}**TS1**$_{cat}$ than in ^{4,2}**TS1**$_{IV}$ as indicative of a transition state *en route* to ^{2}**B**$_{cat}$. Despite the fact that ^{2}**B**$_{cat}$ is low in energy, its corresponding transition state for the double electron transfer through C–O bond formation is high in energy; and we located ^{2}**TS1**$_{cat}$ at $\Delta G^{\ddagger}$ = 29.4 kcal mol^{-1}. Nevertheless, the calculated C–O bond activation barriers for ^{4,2}**TS1**$_{IV}$ compare well with those previously reported for aromatic hydroxylation reactions by P450 CpdI which also gave close energy barriers for the doublet and quartet spin states.[24] We did attempt to swap molecular orbitals and find lower energy transition state structures for alternative radical pathways on the iron(III) surface and characterized ^{4}**TS1**$_{III}$. However, even though ^{4}**TS1**$_{III}$ is electronically different from ^{4}**TS1**$_{IV}$ and ^{2}**TS1**$_{cat}$ (see spin densities in Supporting Information Table S3) it still is well above the reactants complex by $\Delta G^{\ddagger}$ = 30.6 kcal mol^{-1}.

Geometrically, the transition states (Figure 2) have elongated Fe–O bonds to 1.748 Å in ^{4}**TS1**$_{IV}$, 1.805 Å in ^{2}**TS1**$_{cat}$, and 1.741 Å in ^{2}**TS1**$_{IV}$, while the substrate has approached 1.880 Å in ^{4}**TS1**$_{IV}$, 1.931 Å in ^{2}**TS1**$_{cat}$ and 1.925 Å in ^{2}**TS1**$_{IV}$. Although the C–F bond has been displaced from the plane of the aromatic ring, the distance is virtually the same as in the reactants complex. The imaginary frequency in the C–O bond activation transition states is relatively large, i.e., i590 cm^{-1} for ^{4}**TS1**$_{IV}$, i618 cm^{-1} for ^{2}**TS1**$_{cat}$, and i522 cm^{-1} for ^{2}**TS1**$_{IV}$. Typical values for aromatic hydroxylation C–O bond formation transition state imaginary frequencies are in the range between 200 – 600 cm^{-1}.[24,25]

Subsequently, from the **B**-type structures we explored a reaction mechanism for a C–F cleavage barrier via transition state **TS2** to form the defluorinated sunitinib product **C**, where the fluorine has transferred from substrate to the iron and formed a stable Fe–F bond. Optimized transition state structures **TS2** are shown in Figure S12, Supporting Information. Both structures have an imaginary frequency representing the C–F–Fe stretch vibration with magnitude i295 cm^{-1} for ^{4}**TS2**$_{IV}$ and i304 cm^{-1} for ^{2}**TS2**$_{cat}$. As such, both vibrations represent the transfer of fluorine atoms from the substrate to iron. The Fe–F distance has elongated to 2.309 and 2.080 Å in the quartet and doublet spin state transition states, while the oxygen atom originating from CpdI is now at a distance of 3.189 and 4.082 Å from iron, respectively. The Fe–F–C angle is considerably bent at 115° in ^{4}**TS2**$_{IV}$ and 153° in ^{2}**TS2**$_{cat}$, probably due to substrate constraints in the substrate binding pocket. From the **TS2** structures, the calculations relax to structure **C**$_{IV}$ which is characterized as an iron(IV)-fluorine with radical on the substrate and configuration $\pi^{*}_{xz}{}^{1}$ $\pi^{*}_{yz}{}^{1}$ $a_{2u}{}^{2}$ $\pi_{Sub}{}^{1}$ configuration. The electronic configuration of ^{4,2}**C**$_{IV}$ is similar to that of ^{4,2}**B**$_{IV}$. On both spin states a considerable barrier is found

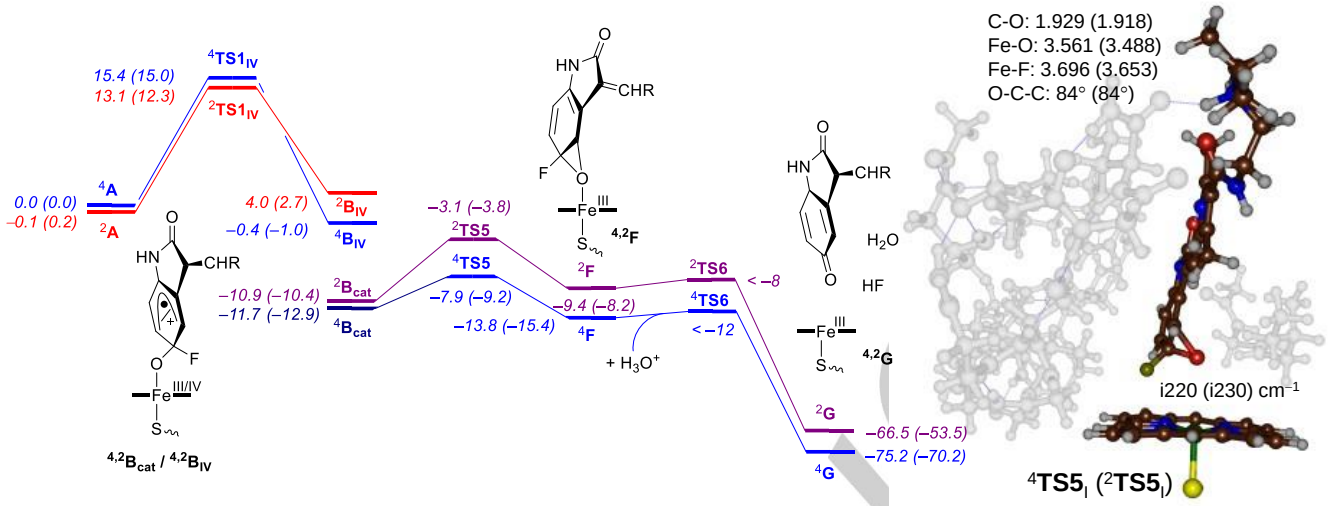

Figure 3. Sunitinib defluorination reaction via an epoxide intermediate by a large CYP 1A2 cluster model of 367 atoms as calculated with DFT approaches. Energies are UB3LYP/BS2//UB3LYP/BS1 values in kcal mol^{-1} corrected with zero-point energies, while free energies at 298 K are in parenthesis. Optimized transition state structures give bond lengths in Å and the imaginary frequency in cm^{-1}.

for this defluorination transition state, which is not surprising as a strong C–F bond is broken. Thus, on the quartet spin state, ^{4}**TS2**$_{IV}$ is located at $\Delta G^{\ddagger}$ = 13.9 kcal mol^{-1} above the reactant complex, whereas the ^{2}**TS2**$_{cat}$ structure is at $\Delta G^{\ddagger}$ = 14.9 kcal mol^{-1}. Despite the fact that ^{4}**B**$_{cat}$ is the lowest energy **B**-type structure, its defluorination barrier is high and located at ΔG = 21.4 kcal mol^{-1}. As ^{2}**B**$_{cat}$ is more stable than the reactants by ΔG = 10.4 kcal mol^{-1}, this implies the ^{2}**TS2**$_{cat}$ barrier is 25.3 kcal mol^{-1} with respect to ^{2}**B**$_{cat}$, while the ^{4}**TS2**$_{cat}$ barrier is 34.3 kcal mol^{-1} with respect to ^{4}**B**$_{cat}$. These high energy barriers highlight that the defluorination step via **TS2** will be slow and rate-determining rather than the initial C–O bond activation as usually seen in aromatic hydroxylation reactions.[24,25] Therefore, we searched for alternative pathways of sunitinib defluorination at the heme center of P450 1A2. For both doublet and quartet spin, we also characterized the iron(III)heme(cation radical) states with orbital occupation $\pi^{*}_{xz}{}^{2}$ $\pi^{*}_{yz}{}^{1}$ $a_{2u}{}^{1}$ $\pi_{Sub}{}^{1}$ configuration, but these states were higher in energy than the iron(IV)-states for the quartet spin state by 4 kcal mol^{-1}. We attempted to swap molecular orbitals and find the ^{2}**C**$_{cat}$ intermediate with configuration $\pi^{*}_{xz}{}^{2}$ $\pi^{*}_{yz}{}^{1}$ $a_{2u}{}^{2}$ $\pi_{Sub}{}^{0}$ with either an anionic substrate or cationic substrate moiety; however, during the self-consistent field calculations, these states converged back to ^{2}**C**$_{IV}$ instead. Consequently, ^{2}**C**$_{cat}$ is well higher in energy than ^{2}**C**$_{IV}$.

Next, we searched for pathways to convert intermediates **C** into final quinoneimine or phenol products. Firstly, we attempted a direct release of F^{-} from the iron center in ^{4,2}**C**$_{IV}$ to form ^{4,2}**E** (Scheme 2). To this end, we ran constraint geometry scans whereby all degrees of freedom were minimized except the Fe–F distance that was elongated from the optimized value in **C** to a value of around 2.3 Å. However, these scans were found to have high barriers via ^{4,2}**TS4** of well over 25 kcal mol^{-1} with respect to ^{2,4}**C**$_{IV}$ (see Supporting Information Figure S9). As such, fluorine release from iron in structure **C** will not likely happen easily. We then attempted several alternative mechanisms by focusing on sunitinib protonation and deprotonation in structure ^{4,2}**C** instead. Thus, either sunitinib can pick up a proton from the environment to give a phenol product (pathway via **TS3** leading to **D**) or alternatively releases the proton from the N–H group to a water molecule to form the quinoneimine product (pathway via **TS3'** to give **D'**). Therefore, for the phenol-formation pathway, we took the optimized geometries of ^{4,2}**C**$_{IV}$ and manually added an H_3O^{+} and water molecule to the model in hydrogen bonding distance to the ketone group of sunitinib, designated structure **C**•(H_2O)(H_3O^{+}). Thereafter, a proton transfer scan was run to transfer one of the protons of H_3O^{+} to the oxygen atom of the sunitinib substrate. However, this scan continuously went up in energy and never crossed a barrier leading to a local minimum (Figure S6, Supporting Information). As a consequence, the phenol formation pathway is impossible from structure ^{4,2}**C** and the channel via **TS3** does not exist. From the same structure also a proton transfer from H_3O^{+} to fluorine was attempted, however, no stable local minimum for fluorine release from the iron center was found (Supporting Information, Figure S7).

Subsequently, we added water molecules nearby the N–H group of sunitinib substrate instead (structure **C**•(H_2O)$_3$) and followed the pathway via **TS3'** to give quinoneimine products. Also, this pathway did not lead to a local minimum for **D'** and resulted in a continuous increase in energy, as shown in the Supporting Information Figure S8. Consequently, the pathway via **TS3'** and **D'** can be ruled out as a possible reaction mechanism.

To find a more viable mechanism for oxygen atom transfer and defluorination of sunitinib by P450 1A2 isozymes, we then explored a pathway starting with substrate epoxidation, and its energy landscape is shown in Figure 3. Similarly to the mechanism discussed in Figure 2, the epoxidation mechanism starts with C–O bond activation to form the **B** structures but then continues with ring-closure to form the epoxide intermediate ^{4,2}**F** via transition state **TS5**. We located transition states at the doublet and quartet spin states, see Figure 4, whereby the doublet spin barrier is $\Delta G^{\ddagger}$ = 6.6 kcal mol^{-1} above the energy of ^{2}**B**$_{cat}$, while the ^{4}**TS5** barrier is $\Delta G^{\ddagger}$ = 3.7 kcal mol^{-1} above ^{4}**B**$_{cat}$. Overall, these ring-closure barriers are well lower in energy than the competing

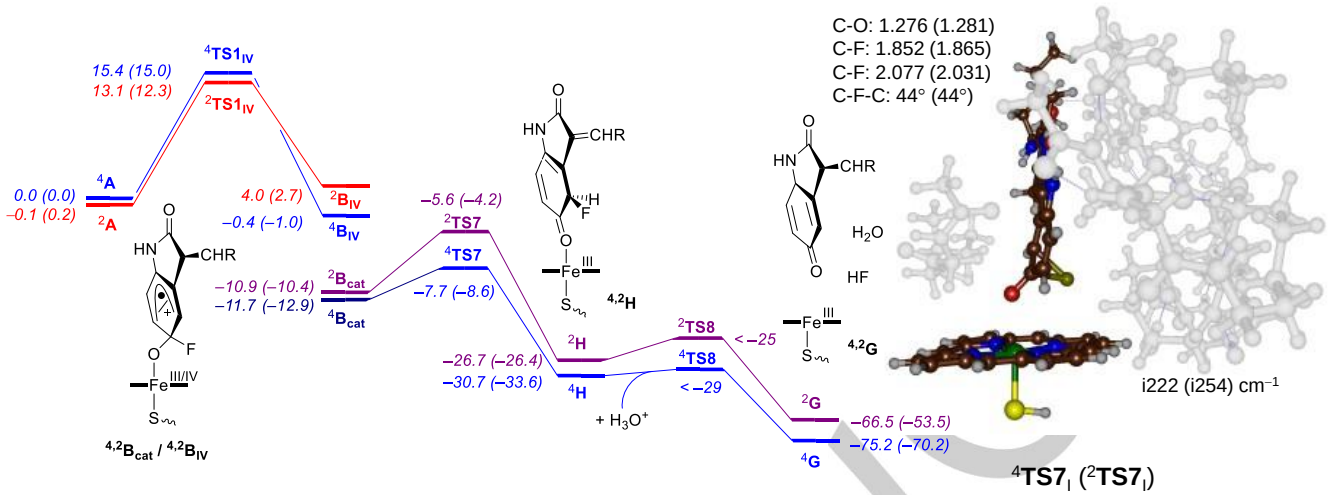

Figure 4. Sunitinib defluorination reaction via 1,2-fluorine transfer by a large CYP 1A2 cluster model of 367 atoms as calculated with DFT approaches. Energies are UB3LYP/BS2//UB3LYP/BS1 values in kcal mol^{-1} corrected with zero-point energies, while free energies at 298 K are in parenthesis. Optimized transition state structures give bond lengths in Å and the imaginary frequency in cm^{-1}.

defluorination barriers via **TS2** and hence epoxidation will be a fast reaction pathway for P450 activation of sunitinib. It should be noted that two isomeric epoxides can be formed, namely bridging carbon atoms C_3 and C_4 or bridging C_4 and C_5 atoms. Calculations were run for ring-closure geometry scans in both directions and either scan gives a low barrier pathway. Consequently, isomeric epoxide intermediate structures can be formed.

Optimized transition state structures for epoxidation ring-closure ^{4,2}**TS5** are shown in Figure 3. Both doublet and quartet spin transition states have an imaginary frequency for the C–C–O bend motion with magnitudes of i220 (quartet) and i230 (doublet) cm^{-1}. The C–C–O angle in both transition states is 84°, while the bond forming C–O distance is at 1.929 (quartet) and 1.918 (doublet) Å. The epoxide is not bound to iron anymore with neither the oxygen nor the fluorine atoms as both distances in the two transition states are well longer than 3 Å. The epoxide product complexes ^{4,2}**F** have unpaired spin density solely based on the iron heme groups with no radical character on the substrate remaining. As the **TS2** barriers for direct cleavage of the C–F bond are high in energy, we investigated the defluorination of the epoxide products by adding an H_3O^+ molecule to the substrate binding pocket nearby the fluorine atom in ^{4,2}**F**. Upon geometry optimization, however, the fluorine atom abstracts a proton and is released from the sunitinib structure. Therefore, the C–F bond in the epoxide intermediate is weak and is easily cleaved to form the strong H–F bond. No barrier was found to fluorine release from the epoxide intermediate. In conclusion, the ^{4,2}**B**$_{cat}$ structures when formed, rapidly rearrange the substrate to the epoxide and followed by a barrierless defluorination assisted by an H_3O^+ ion give quinoneimine products.

Early studies on small model complexes suggested that the oxidation of haloaromatic compounds by the P450s is triggered through a 1,2-halogen transfer reaction.[14] To test this mechanism, we explored possible 1,2-fluorine shifts in ^{4,2}**B**$_{cat}$, and the obtained potential energy profile is shown in Figure 4. On the quartet spin state surface, a small barrier via ^{4}**TS7** of $\Delta G^‡$ = 4.3 kcal mol^{-1} above ^{4}**B**$_{cat}$ transfers the fluorine to the neighboring carbon atom to form ^{4}**H** with large exergonicity (^{4}**H** is ΔG = –33.6 kcal mol^{-1} below ^{4}**A**). On the doublet spin state, the fluorine transfer barrier is somewhat higher in free energy than on the quartet spin state, namely ^{2}**TS7** is 6.2 kcal mol^{-1} above ^{2}**B**$_{cat}$. Both barriers are well lower in energy than the defluorination barriers from Figure 2 (via ^{4,2}**TS2**) and of a similar order of magnitude as the epoxide defluorination barrier in Figure 3 (via ^{4,2}**TS5**). Consequently, the epoxide defluorination will be competitive with 1,2-fluorine migration. Nevertheless, both pathways converge to the quinoneimine products via barrierless subsequent transition states and the assistance of an H_3O^+ group.

Optimized transition state structures ^{4,2}**TS7** are shown on the right-hand side of Figure 4. The imaginary frequencies are small at i222 and i254 cm^{-1}; however, for the same process by an oxo-bridged diiron porphyrin system, a value of i122 cm^{-1} was observed.[26] The transitions are relatively central with the donating C–F bond at 1.852 and 1.865 Å and the accepting C–F bond at 2.077 and 2.031 Å in ^{4}**TS7** and ^{2}**TS7**, respectively. After ^{4,2}**TS7** the system relaxes to ketone intermediates ^{4,2}**H**. We then added an H_3O^+ molecule to the model and studied defluorination and the formation of HF and quinoneimine products via transition state **TS8**. This reaction has a large exergonicity and a small transition state leading to products **G**. From **G**, we calculated the deprotonation of the N–H group of the substrate to give the final quinoneimine product **K**; however, this barrier was negligible.

To explain and understand the electron transfer processes during the reaction mechanism, we devised a valence bond (VB) diagram on the valence orbitals and electrons in Figure 5. These VB diagrams explain the electronic configuration of structures and the bond breaking, bond forming and electron transfer processes that happen in the reaction mechanism.[27] This Figure shows electrons with a dot and the spin direction with an up or down arrow, while a line ending with a dot on each end represents a doubly occupied bonding orbital between those two atoms. Thus, CpdI has an orbital occupation $\pi^*_{xz}{}^1$ $\pi^*_{yz}{}^1$ $a_{2u}{}^1$ and a closed-shell substrate set of orbitals (π_{Sub}). The CpdI valence orbitals can be seen as two 2-center-3-electron bonds along the Fe–O axis in the xz and yz molecular planes. The electrophilic addition of CpdI to the aromatic ring forms a C–O molecular orbital (σ_{CO}) between one of the π_{xz} electrons along the Fe–O bond with an electron from the aromatic ring. The π_{xz} and π^*_{xz} orbitals along the Fe–O

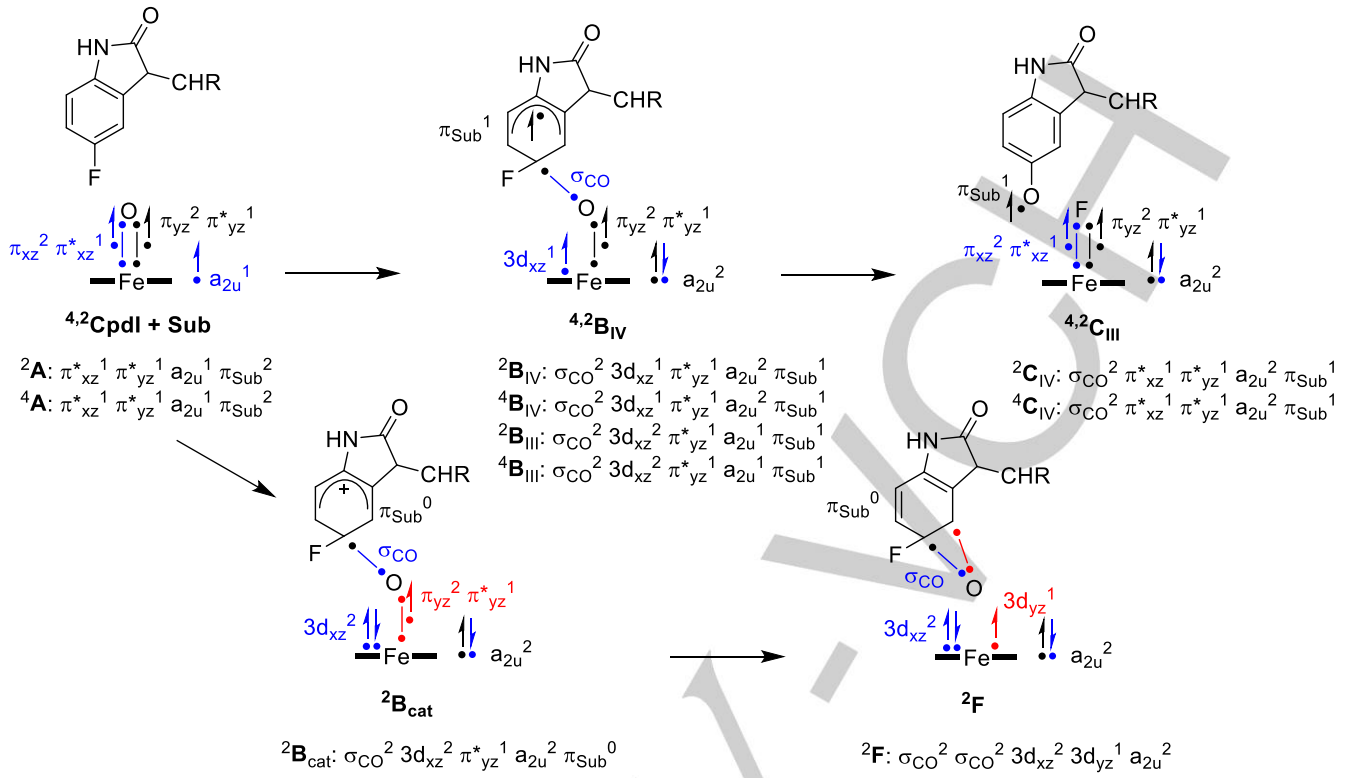

Figure 5. Valence bond description of the electron transfer processes involved in the process from **A** to **C** and **A** to **F** in the reaction mechanisms. A dot represents an electron, while a line separating two dots is a chemical bond shared by two electrons. Electronic configurations are given underneath each structure.

bond have three electrons in CpdI: one pairs up with a 2p electron of the aromatic ring to form the σ_{CO} bond, the second one is transferred to the a_{2u} orbital, while the third one remains as a lone pair orbital on iron in $3d_{xz}$ in the ^{4,2}**B**$_{IV}$ electronic state as highlighted in blue in Figure 5. The alternative ^{4,2}**B**$_{III}$ states have the $3d_{xz}$ orbital doubly occupied and the a_{2u} orbital singly occupied instead. A fifth electromer of structure **B**, i.e., ^{2}**B**$_{cat}$, has the substrate doubly oxidized to a cation ($\pi_{Sub}{}^0$ configuration) coupled to a metal-heme configuration of $3d_{xz}{}^2\ \pi^*_{yz}{}^1\ a_{2u}{}^2$.

We attempted to find the same set of electromers for structures **B** and **C**; however, the binding of fluorine to iron rather than an oxo group dramatically changes the orbital energies, resulting in a Compound II-type configuration with two singly occupied π^* orbitals coupled to a closed-shell heme set of orbitals. In particular, the lone pair $3d_{xz}$ orbital reforms the π_{xz}/π^*_{xz} interaction along the Fe–F bond. In addition, there is considerable mixing of the fluorine orbitals into the a_{2u} orbital. As such, the electronic configuration for **C**$_{IV}$ has orbital occupation $\pi^*_{xz}{}^1\ \pi^*_{yz}{}^1\ a_{2u}{}^2\ \pi_{Sub}{}^1$ while **C**$_{III}$ has orbital occupation $\pi^*_{xz}{}^2\ \pi^*_{yz}{}^1\ a_{2u}{}^1\ \pi_{Sub}{}^1$. The multiple orbital interactions between fluorine and the iron and heme groups will create a strong Fe–F bond, which indeed we find to have a large bond energy for cleavage. This configuration of the structures ^{4,2}**C** leaves a phenoxyl radical on the substrate. We made attempts to swap molecular orbitals to obtain a substrate anion, but the self-consistent-field calculations converged back to the electronic state for ^{4,2}**C** described in Figure 5.

The epoxide intermediate has no radical character on the substrate moiety and is formed from the ^{2}**B**$_{cat}$ intermediate through the breaking of the 2-center-3-electron bond along the Fe–O axis ($\pi_{yz}\ \pi^*_{yz}$) into atomic orbitals. This transfers two electrons in the newly formed C–O bond of the epoxide and leaves one electron on the metal in $3d_{yz}$. In the quartet spin state, the two electrons from $3d_{xz}$ are split and end up in the $3d_{xz}$ and $3d_{z2}$ atomic orbitals. Any subsequent pathway from either the epoxide intermediate or the reaction from ^{4,2}**B**$_{cat}$ via 1,2-fluorine shift does not further change the electronic configuration of the heme and results from either proton or F^- transfer processes.

To gain insight into why a 1,2-fluorine shift is feasible and what structures can cleave the C–F bond the easiest, we calculated bond dissociation energies (BDEs) for the homolytic and heterolytic C–F bond cleavage in various intermediates. Thus, we extracted the substrate moiety from the reactant complex and performed a DFT single-point calculation at the B3LYP/BS2 level of theory. Thereafter, we calculated it again but without $F^\bullet$ (for the homolytic cleavage) or without F^- (for the heterolytic cleavage) from the substrate leading to a radical or cation, respectively. Figure 6 displays calculated homolytic and heterolytic C–F bonds for the isolated substrate, the **B**-type intermediates, the epoxide intermediates, the quinoneimine intermediates as well as the iron(III)-fluoro complex. In the reactants, the BDE for homolytic cleavage of the C–F bond is 125.6 kcal mol^{-1}, whereas heterolytic cleavage requires 162.5 kcal mol^{-1}. These are strong chemical bonds and hence direct C–F bond cleavage will be difficult. However, upon C–O bond formation as in **B**, the carbon atom of the C–F bond changes from sp^2 hybridization to sp^3 hybridization. This considerably weakens the C–F bond strength and its BDE is reduced to 82.6 kcal mol^{-1} for homolytic cleavage and 80.1 kcal mol^{-1} for heterolytic cleavage. These values implicate that both

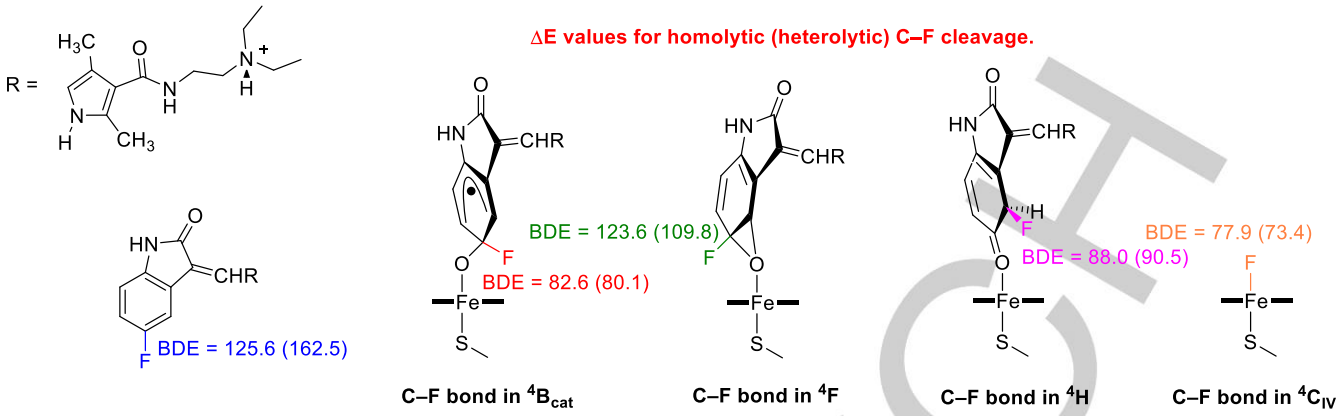

Figure 6. Homolytic and heterolytic C–F bond dissociation energies (BDEs) of selected intermediates and products along the reaction mechanism of aromatic defluorination by P450 Cpd I. Single points done on the optimized geometries with values in kcal mol^{-1}.

homolytic and heterolytic cleavage of the C–F bond are possible and as the C–F bond strength is weakened in ^{4}**B**$_{cat}$ the bond can be broken when a stronger bond is formed in the process. As the Fe–F bond is of similar energy (ΔE = 77.9 kcal mol^{-1} for homolytic cleavage) as the C–F bond in ^{4}**B**$_{cat}$ and there is a major electronic rearrangement upon the conversion of the ^{4}**B**$_{cat}$ into ^{4}**C**$_{IV}$ (see Figure 5) as a result this step incurs a relatively high reaction barrier for defluorination.

We then calculated the C–F BDEs in the epoxide and quinone structures **F** and **H**. In both structures, the C–F bond is weaker than in the reactant structure with heterolytic cleavage energies of 109.8 and 90.5 kcal mol^{-1}, respectively, calculated. These values implicate that 1,2-fluorine transfer in ^{4}**B**$_{cat}$ to form ^{4}**H** is a favorable pathway as it will give a structure with a stronger C–F bond by about 10 kcal mol^{-1}. Indeed, a comparison of the relative energy values of ^{4}**H** and ^{4}**B**$_{cat}$ from Figure 4 gives an exothermic reaction for the 1,2-fluorine shift. Both structures ^{4}**F** and ^{4}**H** have a stronger C–F bond than the Fe–F bond in ^{4}**C**$_{IV}$ and consequently will release these products rather than transfer the fluorine to the iron center. The epoxide and quinoneimine structures can release fluorine in a reaction with a proton in the protein or solution.

Conclusion

To understand the mechanism and feasibility of aromatic defluorination by cytochrome P450 enzymes, we performed a detailed DFT study using a drug molecule (sunitinib) as a model substrate and explored a range of possible reaction mechanisms. We utilized a large cluster model comprised of 367 atoms and conducted extensive density functional theory calculations, commencing from Compound I in both doublet and quartet spin states. The defluorination mechanisms under investigation all are initiated with an electrophilic addition step, and progress to an oxo-bridged complex (**B**), whereby various electronic states and conformations were considered. The most energetically stable **B**-type intermediates were found to be of the iron(III)-type, featuring a cation on the substrate. Subsequent exploration of mechanisms from these intermediates covered direct defluorination, 1,2-fluorine shift, and ring-closure to form an epoxide. The latter two pathways exhibited low energy barriers, making them plausible in an enzymatic environment. The C–F bond in both intermediates showed significant weakening relative to the initial complex, indicating a potential route for defluorination via H_3O^+ interaction. Furthermore, the likelihood of a stable iron(III)-fluoro complex forming within the substrate binding pocket was identified, albeit with a bond strength inferior to that of the substrate C–F bond, thus negating the chance of substantial Fe–F bond formation. As C–Cl, C–Br, and C–I bonds are substantially weaker than an aromatic C–F bond, our results implicate that also other aromatic carbon-halogen bonds can be broken by P450 isozymes, although they may react with a different mechanism.

Acknowledgements

The computational shared facilities (CSF) at the University of Manchester are thanked for providing CPU time for this work.

Keywords: density functional theory • enzyme catalysis • inorganic reaction mechanisms • biocatalysis • hydroxylation

[1] a) J. Lv, H. Wang, G. Rong, Y. Cheng, *Acc. Chem. Res*. **2022**, *55*, 722−733; b) P. Jeschke, *Eur. J. Org. Chem*. **2022**, *2022*, e202101513; c) C. Zhang, K. Yan, C. Fu, H. Peng, C. J. Hawker, A. K. Whittaker, *Chem. Rev*. **2022**, *122*, 167−208.

[2] T. Fujita, K. Fuchibe, J. Ichikawa, *Angew. Chem. Int. Ed*. **2019**, *58*, 390−402.

[3] O. Eisenstein, J. Milani, R. N. Perutz, *Chem. Rev*. **2017**, *117*, 8710−8753.

[4] a) J. Serrano-Plana, I. Garcia-Bosch, R. Miyake, M. Costas, A. Company, *Angew. Chem. Int. Ed*. **2014**, *53*, 9608−9612; b) C. Colomban, E. V. Kudrik, P. Afanasiev, A. B. Sorokin, *J. Am. Chem. Soc*. **2014**, *136*, 11321−11330; c) C. Colomban, E. V. Kudrik, A. B. Sorokin, *J. Porph. Phthalocyanin*. **2017**, *21*, 345−353.

[5] a) W. Tong, Q. Huang, M. Li, J.-B. Wang, *Bioresour. Bioprocess*. **2019**, *6*, 46; b) H. J. Seong, S. W. Kwon, D.-C. Seo, J.-H. Kim, Y.-S. Jang, *Appl. Biol. Chem*. **2019**, *62*, 621 c) Y. Wang, A. Liu, *Chem. Soc. Rev*. **2020**, *49*, 4906−4925; d) M. Costas, A. Company, *Eur. J. Inorg. Chem*. **2022**, *2022*, e202100754; e) A. Timmins, S. P. de Visser, *Catalysts* **2018**, *8*, 314.

[6] a) P. J. Hillas, P. F. Fitzpatrick, *Biochemistry* **1996**, *35*, 6969−6975; b) W. Singh, S. F. G. Santos, S. Yadav, G. W. Black, K. D. Dubey, *Biochemistry* **2023**, *62*, 1577-1587.

[7] a) Y. Wang, I. Davis, I. Shin, D. J. Wherritt, W. P. Griffith, K. Dornevil, K. L. Colabroy, A. Liu, *ACS Catal*. **2019**, *9*, 4764−4776; b) T. Malewschik, R. A. Ghiladi, *Coord. Chem. Rev*. **2021**, *441*, 213976.

[8] a) E. D. Kharasch, K. E. Thummel, *Anesthesiology* **1993**, *79*, 795-807; b) I. M. C. M. Rietjens, C. den Besten, R. P. Hanzlik, P. J. van Bladeren, *Chem. Res. Toxicol*. **1997**, *10*, 629−635; c) P. J. Mutch, G. J. Dear, I. M. Ismail, *J. Pharmacy Pharmacol.* **2001**, *53*, 403-408; d) A. Harkey, H.-J. Kim, S. Kandagatla, G. M. Raner, *Biotechnol. Lett*. **2012**, *34*, 1725-1731; e) Q. Huang, X. Zhang, Q. Chen, S. Tian, W. Tong, W. Zhang, Y. Chen, M. Ma, B. Chen, B. Wang, J.-b. Wang, *ACS Catal*. **2022**, *12*, 265−272; f) T. Coleman, M. N. Podgorski, M. L. Doyle, J. M. Scaffidi-Muta, E. C. Campbell, J. B. Bruning, J. J. De Voss, S. G. Bell, *J. Inorg. Biochem*. **2023**, *244*, 112234.

[9] a) G. M. Amaya, R. Durandis, D. S. Bourgeois, J. A. Perkins, A. A. Abouda, K. J. Wines, M. Mohamud, S. A. Starks, R. N. Daniels, K. D. Jackson, *Chem. Res. Toxicol*. **2018**, *31*, 570−584; b) E. A. Burnham, A. A. Abouda, J. E. Bissada, D. T. Nardone-White, J. L. Beers, J. Lee, M. J. Vergne, K. L. Jackson, *Chem. Res. Toxicol*. **2022**, *35*, 792−806.

[10] a) M. Sono, M. P. Roach, E. D. Coulter, J. H. Dawson, *Chem. Rev*. **1996**, *96*, 2841−2888; b) *Handbook of Porphyrin Science*, (Eds.: K. M. Kadish, K. M. Smith, R. Guilard), World Scientific Publishing Co., New Jersey, **2010**; c) *Iron-containing enzymes: Versatile catalysts of hydroxylation reaction in nature* (Eds.: S. P. de Visser, D. Kumar), RSC Publishing, Cambridge (UK), **2011**; d) P. R. Ortiz de Montellano, *Chem. Rev*. **2010**, *110*, 932−948; e) B. Meunier, S. P. de Visser, S. Shaik, *Chem. Rev*. **2004**, *104*, 3947−3980; f) X. Huang, J. T. Groves, *Chem. Rev*. **2018**, *118*, 2491−2553; g) H. M. Girvan, A. W. Munro, *Curr. Opin. Chem. Biol*. **2016**, *31*, 136−145; h) I. G. Denisov, T. M. Makris, S. G. Sligar, I. Schlichting, *Chem. Rev.* **2005**, *105*, 2253−2277; i) M. T. Green, *Curr. Opin. Chem. Biol*. **2009**, *13*, 84−88; j) N. P. Dunham, F. H. Arnold, *ACS Catal*. **2020**, *10*, 12239−12255; k) T. L. Poulos, A. H. Follmer, *Acc. Chem. Res*. **2022**, *55*, 373−380.

[11] F. P. Guengerich, *ACS Catal*. **2018**, *8*, 10964−10976.

[12] a) J. Guo, X. Zhu, S. Badawy, A. Ihsan, Z. Liu, C. Xie, X. Wang, *Curr. Drug Metab.* **2021**, *22*, 40-49; b) T. Mokkawes, S. P. de Visser, *Chem. Eur. J*. **2023**, *29*, e202203875.

[13] a) S. Shaik, D. Kumar, S. P. de Visser, A. Altun, W. Thiel, *Chem. Rev*. **2005**, *105*, 2279−2328; b) D. Li, Y. Wang, K. Han, *Coord. Chem. Rev*. **2012**, *256*, 1137−1150; c) M. N. Podgorski, T. Coleman, R. R. Chao, J. J. De Voss, J. B. Bruning, S. G. Bell, *J. Inorg. Biochem*. **2020**, *203*, 110913; d) U. K. Bagha, J. K. Satpathy, G. Mukherjee, P. Barman, D. Kumar, S. P. de Visser, C. V. Sastri, *Farad. Disc*. **2022**, *234*, 58-69; e) U. K. Bagha, R. Yadav, T. Mokkawes, J. K. Satpathy, D. Kumar, C. V. Sastri, S. P. de Visser, *Chem. Eur. J*. **2023**, *29*, e202300478.

[14] J. C. Hackett, T. T. Sanan, C. M. Hadad, *Biochemistry* **2007**, *46*, 5924−5940.

[15] a) S. Sansen, J. K. Yano, R. L. Reynald, G. A. Schoch, K. J. Griffin, C. D. Stout, E. F. Johnson, J. *Biol. Chem*. **2007**, *282*, 14348−14355; b) H. M. Berman, J. Westbrook, Z. Feng, G. Gilliland, T. N. Bhat, H. Weissig, I. N. Shindyalov, P. E. Bourne, *Nucl. Acids Res*. **2000**, *28*, 235−242.

[16] O. Trott, A. J. Olson, *J. Comput. Chem.* **2010,** *31*, 455−461.

[17] E. F. Pettersen, T. D. Goddard, C. C. Huang, G. S. Couch, D. M. Greenblatt, E. C. Meng, T. E. Ferrin, *J. Comput. Chem*. **2004**, *25*, 1605−1612.

[18] a) A. Timmins, M. Saint-André, S. P. de Visser, *J. Am. Chem. Soc*. **2017**, *139*, 9855–9866; b) H. S. Ali, S. P. de Visser, *Chem. Eur. J*. **2022**, *28*, e202104167; c) H. S. Ali, J. Warwicker, S. P. de Visser, *ACS Catal*. **2023**, *13*, 10705–10721.

[19] a) J. Rittle, M. T. Green, *Science* **2010**, *330*, 933−937; b) K. D. Dubey, S. Shaik, *Acc. Chem. Res*. **2019**, *52*, 389−399; c) S. P. de Visser, Y.-T. Lin, H. S. Ali, U. K. Bagha, G. Mukherjee, C. V. Sastri, *Coord. Chem. Rev*. **2021**, *43*9, 213914.

[20] a) M. T. Green, *J. Am. Chem. Soc*. **1999**, *121*, 7939−7940; b) J. C. Schöneboom, H. Lin, N. Reuter, W. Thiel, S. Cohen F. Ogliaro, S. Shaik, *J. Am. Chem. Soc*. **2002**, *124*, 8142−8151; c) S. P. de Visser, S. Shaik, P. K. Sharma, D. Kumar, W. Thiel, *J. Am. Chem. Soc*. **2003**, *125*, 15779−15788; d) C. M. Bathelt, J. Zurek, A. J. Mulholland, J. N. Harvey, *J. Am. Chem. Soc*. **2005**, *127*, 12900−12908; e) C. S. Porro, M. J. Sutcliffe, S. P. de Visser, *J. Phys. Chem. A* **2009**, *113*, 11635−11642; f) M. Radoń, E. Broclawik, K. Pierloot, *J. Chem. Theory Comput*. **2011**, *7*, 898−908; g) R. Lonsdale, J. Oláh, A. J. Mulholland, J. N. Harvey, *J. Am. Chem. Soc*. **2011**, *133*, 15464−15474; h) M. G. Quesne, D. Senthilnathan, D. Singh, D. Kumar, P. Maldivi, A. B. Sorokin, S. P. de Visser, *ACS Catal*. **2016**, *6*, 2230−2243; i) K. P. Kepp, *Phys. Chem. Chem. Phys*. **2017**, *19*, 22355−22362; j) X.-X. Li, V. Postils, W. Sun, A. S. Faponle, M. Solà, Y. Wang, W. Nam, S. P. de Visser, *Chem. Eur. J*. **2017**, *23*, 6406−6418; k) H. Su, G. Ma, Y. Liu, *Inorg. Chem*. **2018**, *57*, 11738−11745; l) A. Spinello, M. Pavlin, L. Casalino, A. A. Magistrato, *Chem. Eur. J*. **2018**, *24*, 10840−10849; m) Q. M. Phung, K. Pierloot, *J. Chem. Theory Comput*. **2019**, *15*, 3033−3043; n) H. S. Ali, R. H. Henchman, S. P. de Visser, *Chem. Eur. J*. **2020**, *26*, 13093−13102; o) S. Louka, S. M. Barry, D. J. Heyes, M. Q. E. Mubarak, H. S. Ali, L. M. Alkhalaf, A. W. Munro, N. S. Scrutton, G. L. Challis, S. P. de Visser, *J. Am. Chem. Soc*. **2020**, *142*, 15764–15779; p) Q. Cheng, N. J. DeYonker, *J. Phys. Chem. B* **2021**, *125*, 3296−3306.

[21] S. Shaik, S. P. de Visser, F. Ogliaro, H. Schwarz, D. Schröder, *Curr. Opin. Chem. Biol*. **2002**, *6*, 556−567.

[22] a) S. P. de Visser, F. Ogliaro, P. K. Sharma, S. Shaik, *J. Am. Chem. Soc*. **2002**, *124*, 11809–11826; b) J. C. Schöneboom, S. Cohen, H. Lin, S. Shaik, W. Thiel, *J. Am. Chem. Soc*. **2004**, *126*, 4017–4034.

[23] a) S. P. de Visser, *Chem. Eur. J*. **2020**, *26*, 5308–5327; b) G. Mukherjee, J. K. Satpathy, U. K. Bagha, M. Q. E. Mubarak, C. V. Sastri, S. P. de Visser, *ACS Catal*. **2021**, *11*, 9761–9797; c) S. P. de Visser, G. Mukherjee, H. S. Ali, C. V. Sastri, *Acc. Chem. Res*. **2022**, 55, 65-74.

[24] a) S. P. de Visser, S. Shaik, *J. Am. Chem. Soc*. **2003**, *125*, 7413–7424; b) S. Shaik, P. Milko, P. Schyman, D. Usharani, H. Chen, *J. Chem. Theory Comput*. **2011**, *7*, 327–339; c) D. Kumar, G. N. Sastry, S. P. de Visser, *J. Phys. Chem. B* **2012**, *116*, 718–730.

[25] a) S. P. de Visser, *Chem. Eur. J*. **2006**, *12*, 8168–8177; b) C. M. Bathelt, A. J. Mulholland, J. N. Harvey, *J. Phys. Chem. A* **2008**, *112*, 13149–13156; c) F. G. Cantú Reinhard, M. A. Sainna, P. Upadhyay, G. A. Balan, D. Kumar, S. Fornarini, M. E. Crestoni, S. P. de Visser, *Chem. Eur. J*. **2016**, *22*, 18608–18619; d) M. Asaka, H. Fujii, *J. Am. Chem. Soc*. **2016**, *138*, 8048–8051; e) C. Yuan, Q. Ouyang, X. Wang, X. Li, H. Tan, G. Chen, *Inorg. Chem*. **2021**, *60*, 6433-6445; f) A. Hermano Sampaio Dias, R. Yadav, T. Mokkawes, A. Kumar, M. S. Skaf, C. V. Sastri, D. Kumar, S. P. de Visser, *Inorg. Chem*. **2023**, *62*, 2244-2256.

[26] C. Colomban, A. H. Tobing, G. Mukherjee, C. V. Sastri, A. B. Sorokin, S. P. de Visser, *Chem. Eur. J*. **2019**, *25*, 14320–14331.

[27] a) H. S. Ali, R. H. Henchman, J. Warwicker, S. P. de Visser, *J. Phys. Chem. A* **2021**, *125*, 1720-1737; b) E. F. Gérard, V. Yadav, D. P. Goldberg, S. P. de Visser, *J. Am. Chem. Soc*. **2022**, *144*, 10752-10767.

Entry for the Table of Contents

Graphic for Table of Contents (11.5 cm x 2.5 cm size):

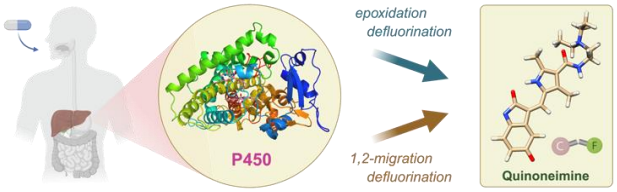

Insert text for Table of Contents here: Density functional calculations establish a novel mechanism of aromatic defluorination by P450 Compound I via either an initial epoxide intermediate or through a 1,2-fluorine shift in an electrophilic intermediate, which highlights that the P450s can defluorinate fluoroarenes. However, in the absence of a proton donor a strong Fe–F bond is formed.

Institute and/or researcher Twitter usernames: The University of Manchester (@OfficialUoM); Department of Chemical Engineering (@UoMSciEng); Manchester Institute of Biotechnology (@UoMMIB).